PHYSICAL REVIEW C **95**, 034307 (2017)

Shell evolution above $Z,N = 50$ within Skyrme density functional theory: The impact of deformation and tensor interactions

Yue Shi (石跃)[*]

Department of Physics, Harbin Institute of Technology, Harbin 150001, People's Republic of China;
National Superconducting Cyclotron Laboratory, Michigan State University, East Lansing, Michigan, 48824-1321, USA;
and Department of Physics, Post Office Box 35 (YFL), FI-40014 University of Jyväskylä, Finland

(Received 31 October 2016; revised manuscript received 6 February 2017; published 10 March 2017)

Background: Recent years have seen considerable effort in associating the shell evolution (SE) for a chain of isotones or isotopes with the underlying nuclear interactions. In particular, it has been fairly well established that the tensor part of the Skyrme interaction is indispensable for understanding certain SE above $Z,N = 50$ shell closures, as a function of nucleon numbers.

Purpose: The purpose of the present work is twofold: (1) to study the effect of deformation due to blocking on the SE above $Z,N = 50$ shell closures and (2) to examine the optimal parametrizations in the tensor part which gives a proper description of the SE above $Z,N = 50$ shell closures.

Methods: I use the Skyrme-Hartree-Fock-Bogoliubov (SHFB) method to compute the even-even vacua of the $Z = 50$ isotopes and $N = 50$ isotones. For Sb and odd-A Sn isotopes, I perform calculations with a blocking procedure which accounts for the polarization effects, including deformations.

Results: The blocking SHFB calculations show that the light odd-A Sb isotopes, with only one valence proton occupying down-sloping $\Omega = 11/2^-$ and $\Omega = 7/2^+$ Nilsson orbits, assume finite oblate deformations. This reduces the energy differences between $11/2^-$ and $7/2^+$ states by about 500 keV for ${}_{51}\mathrm{Sb}_{56-66}$, bringing the energy-difference curve closer to the experimental one. With UNE2T1 energy density functional (EDF), which differs from UNEDF2 parametrization by tensor terms, a better description of the slope of $\Delta e(\pi 1h_{11/2} - \pi 1g_{7/2})$ as a function of neutron number has been obtained. However, the trend of $\Delta e(\pi 1g_{7/2} - \pi 2d_{5/2})$ curve is worse using UNE2T1 EDF. $\Delta e(\nu 3s_{1/2} - \nu 2d_{5/2})$ and $\Delta e(\nu 1g_{7/2} - \nu 2d_{5/2})$ curve for $N = 50$ isotones using UNE2T1 seems to be consistent with experimental data. The neutron SE of $\Delta e(\nu 1h_{11/2} - \nu 1g_{7/2})$ and $\Delta e(\nu 1g_{7/2} - \nu 2d_{5/2})$ for Sn isotopes are shown to be sensive to α_T tensor parameter.

Conclusions: Within the Skyrme self-consistent mean-field model, the deformation degree of freedom has to be taken into account for Sb isotopes, $N = 51$ isotones, and odd-A Sn isotopes when discussing variation of quantities like shell gap etc. The tensor terms are important for describing the strong variation of $\Delta E(\Omega^\pi = 11/2^- - 7/2^+)$ in Sb isotopes. The SE of $1/2^+$ and $7/2^+$ states in $N = 51$ isotones may show signature for the existence of tensor interaction. The experimental excitation energies of $11/2^-$ and $7/2^+$ states in odd-A Sn isotopes close to ${}^{132}\mathrm{Sn}$ give prospects for constraining the α_T parameter.

DOI: 10.1103/PhysRevC.95.034307

I. INTRODUCTION

The underlying single-particle (s.p.) shell structure is of vital importance for understanding a variety of phenomena related to low-energy nuclear structure physics. For example, the discontinuity of two nucleon separation energy and the sudden rise in energy of the 2^+ state at certain nucleon number can be associated with the occurrence of magic numbers. After incorporating a large spin-orbit (SO) term in the Hamiltonian, the nuclear independent mean-field model was found to be able to reproduce the magic numbers seen experimentally along the valley of β stability [1,2]. Since then, various mean-field models have achieved great success in describing properties of the ground states (g.s.) and the near-yrast excited states for nuclei across the nuclear chart.

With recent advances in the experimental techniques [3,4], it has been seen that neutron-rich nuclei with extremely large N/Z ratios can have shell structures which are considerably different from their respective stable isotopes or isotones. The shell variation (evolution) with nucleon number can be so drastic that one sees the disappearance of the conventional shell gaps (magic number) or the appearance of new ones in those exotic systems. This challenges the current mean-field models, which predict rather smooth shell variations when changing the nucleon number, indicating defects in parametrizations, or even missing terms that have not been carefully examined before in the mean-field models.

In particular, the observed trend of the shell evolution (SE) for states above $Z,N = 50$ [3,5] can be consistently explained by including, in the effective shell model [6], a specific tensor contribution. This triggered a number of theoretical mean-field [7–16] and beyond mean-field studies [17–20]. The conclusion is that the tensor part of the interaction is essential for understanding SE [21].

However, although the interplay between deformation and tensor terms has been studied in Ref. [12], a realistic analysis has never been done with deformation effects included. Indeed, experimental observables are extracted from $Z = 51$ nuclei while, to my knowledge, most existing analysis are based on the s.p. states from mean-field calculations for the even-even

---

[*] Corresponding author: yueshi@hit.edu.cn

©2017 American Physical Society

cores which are calculated to be spherical. Experimentally extracted s.p. levels are mostly model dependent. It has been noted in Ref. [22], that even for spherical nuclei, correlations beyond mean field have to be taken into account in the correlated systems. With only one proton outside the $Z = 50$ core, the system may assume prolate or oblate deformation due to the occupation of down-sloping orbits above the shell closure. One needs to recall that occupying s.p. states having large intrinsic quadrupole moments can polarize the system toward static deformed shapes in odd-mass nuclei [23–25].

In this work, I examine the energy differences for $Z = 51$ isotopes taking into account the effect of deformation. Further, I look into the effect of the tensor part of the parametrization in the description of the SE along $Z = 50$ and $N = 50$ isotopic and isotonic chains. In Sec. II I describe theoretical model used in this work. Sec. III discusses results obtained from the present calculations, and Sec. IV gives the conclusion.

II. THE MODEL

The self-consistent Skyrme-Hartree-Fock-Bogoliubov (SHFB) calculations are performed using the density functional theory solver HFBTHO [26]. The HFB equations are solved by expanding the s.p. wave functions in the spherical harmonic-oscillator (HO) basis up to $N_{\max} = 18$. The frequency of the HO basis is $\hbar\omega = 10.3959$ MeV.

In the blocking calculations, the time-odd parts of the mean field [27] appear. It has been shown [28,29] that ignoring time-odd parts of the Skyrme energy density functionals (EDFs) invites energy differences of the order of 100–200 keV compared to the energies obtained with time-odd coupling constants determined by Landau parameters or local-gauge invariance [30]. Therefore, in the blocking calculations, I ignore the time-odd mean fields by adopting the equal-filling approximation of the code [26]. The influence of the time-odd part of the tensor term on the moments of inertia of collective rotational bands in superdeformed nuclei has been studied extensively [13].

I use UNEDF1 [31], UNEDF2 [32], and UNEDF1$^{\mathrm{SO}}$ [29] EDFs with the pairing properties (cutoff energies and pairing strengths) provided in their respective original papers.

In this work I intend to probe the tensor part of the Skyrme EDF by comparing the results with the data. In the following I remind briefly the form of tensor terms appearing in the functional and in the mean-field. For details, I refer the readers to Ref. [14,33]. The EDF reads

$$\mathcal{E} = \int d^3\boldsymbol{r}\mathcal{H}(\boldsymbol{r}), \tag{1}$$

where the local energy density $\mathcal{H}(r)$ is a sum of kinetic energy and the potential energy isoscalar ($t = 0$) and isovector ($t = 1$) terms,

$$\mathcal{H}(\boldsymbol{r}) = \frac{\hbar^2}{2m}\tau_0 + \mathcal{H}_0(\boldsymbol{r}) + \mathcal{H}_1(\boldsymbol{r}), \tag{2}$$

with

$$\mathcal{H}_t(\boldsymbol{r}) = \mathcal{H}_t^{\mathrm{even}} + \mathcal{H}_t^{\mathrm{odd}}, \tag{3}$$

and

$$\mathcal{H}_t^{\mathrm{even}} = C_t^{\rho}\rho_t^2 + C_t^{\Delta\rho}\rho_t\Delta\rho_t + C_t^{\tau}\rho_t\tau_t + C_t^{J}\mathbb{J}_t^2 + C_t^{\nabla J}\rho_t\nabla\cdot\boldsymbol{J}_t, \tag{4}$$

$$\mathcal{H}_t^{\mathrm{odd}} = C_t^{s}\boldsymbol{s}_t^2 + C_t^{\Delta s}\boldsymbol{s}_t\cdot\Delta\boldsymbol{s}_t + C_t^{T}\boldsymbol{s}_t\cdot\boldsymbol{T}_t + C_t^{j}\boldsymbol{j}_t^2 + C_t^{\nabla J}\boldsymbol{s}_t\cdot(\nabla\times\boldsymbol{j}_t). \tag{5}$$

The time-even, ρ_t, τ_t, and $\mathbb{J}_t$, and time-odd, $\boldsymbol{s}_t$, $\boldsymbol{T}_t$, and $\boldsymbol{j}_t$, local densities are introduced in Ref. [34].

The SO density $\boldsymbol{J}$ is the vector part of the spin-current tensor density $\mathbb{J}$, that is,

$$\mathbb{J}_{t,\mu\nu} = \tfrac{1}{3}J_t^{(0)}\delta_{\mu\nu} + \tfrac{1}{2}\varepsilon_{\mu\nu\eta}J_{t,\eta} + J_{t,\mu\nu}^{(2)}, \tag{6}$$

with

$$\mathbb{J}_t^2 \equiv \sum_{\mu\nu}\mathbb{J}_{t,\mu\nu}^2 = \frac{1}{3}\big(J_t^{(0)}\big)^2 + \frac{1}{2}\boldsymbol{J}_t^2 + \sum_{\mu\nu}\big(J_{t,\mu\nu}^{(2)}\big)^2. \tag{7}$$

In this work, I pay special attention to the tensor terms appearing in the EDF,

$$\mathcal{H}_T = C_0^J\mathbb{J}_0^2 + C_1^J\mathbb{J}_1^2. \tag{8}$$

It is to be noted that tensor terms in the form of Eq. (8) is not necessarily related to a tensor force proposed by Skyrme [35,36]. However, in the present case, where parity symmetry is conserved, only the term containing vector part ($\boldsymbol{J}$) of $\mathbb{J}^2$ in Eq. (7) survives [11,12]. This allows for a correspondence between the energy densities generated by the tensor terms (Eq. (22) of Ref. [11]), and the usual tensor force characterized by t_e and t_o (Eq. (20) of Ref. [11]).

Although the calculations in the current work are performed without enforcing spherical symmetry, I show tensor terms in the spherical case to see the feature more clearly. A comprehensive discussion of the tensor terms in spherical symmetry can be found in Ref. [11]. In the spherical case, the pseudoscalar $J^{(0)}$ and symmetric-tensor $J_{\mu\nu}^{(2)}$ parts of the tensor terms vanish, with

$$\mathcal{H}_T = \tfrac{1}{2}C_0^J\boldsymbol{J}_0^2 + \tfrac{1}{2}C_1^J\boldsymbol{J}_1^2. \tag{9}$$

Variation of the tensor parts of the EDF over the radial SO densities $J(r)$ gives the tensor contribution to the spherical isoscalar ($t = 0$) and isovector ($t = 1$) SO mean-fields [14],

$$\Delta W^{\mathrm{SO}} = \frac{1}{2r}\big[C_0^J J_0(r) + C_1^J J_1(r)\big]\boldsymbol{L}\cdot\boldsymbol{S}, \tag{10}$$

which can be separated into the neutron and proton contributions to the SO mean fields,

$$\Delta W_n^{\mathrm{SO}} = \frac{1}{2r}[\alpha_T J_n(r) + \beta_T J_p(r)]\boldsymbol{L}\cdot\boldsymbol{S}, \tag{11}$$

$$\Delta W_p^{\mathrm{SO}} = \frac{1}{2r}[\alpha_T J_p(r) + \beta_T J_n(r)]\boldsymbol{L}\cdot\boldsymbol{S}, \tag{12}$$

with

$$\alpha_T = C_0^J + C_1^J, \tag{13}$$

$$\beta_T = C_0^J - C_1^J, \tag{14}$$

and

$$J_q(r) = \frac{1}{4\pi r^3}\sum_{n,j,l}(2j+1)v_{njl}^2 \times\left[j(j+1) - l(l+1) - \frac{3}{4}\right]\psi_{njl}^2(r). \qquad (15)$$

I summarize briefly about the most important feature of tensor parts. From Eq. (15), it is seen [9] that as the lower branch (which has $j_> = l + \frac{1}{2}$) of the two SO partners starts to be filled, the J_q density increases as $[j(j+1) - l(l+1) - \frac{3}{4}] \geqslant 0$ for $l \geqslant 0$. J_q decreases as the energetically higher branch of the SO partner starts to be filled since now $j_< = l - \frac{1}{2}$. Numerically, it turns out [11] that the tensor terms contribute to the SO splitting evolution much more strongly than the effect of the increase of the diffuseness of the density distribution [37,38].

Only in the spherical limit, it becomes clear from Eqs. (11) and (12) that α_T and β_T control how much the tensor terms contribute to the change of SO mean fields, with changing density (or particle number) of the same and different nucleonic types, respectively. Indeed, previous studies mainly focused on the SE of one nucleonic type with the other nucleonic type variation. This has resulted in the fairly well constrained β_T value, leaving, however, α_T less clear [21]. In Sec. III B 5, I will show that the neutron SE above $N = 50$ shell closure, along the odd-A Sn isotopes is sensitive to α_T values. This is the first attempt to constrain α_T parameter.

III. RESULTS AND DISCUSSIONS

A. Influence of deformation effect

In this section, I examine the polarization effects from the valence proton for the $_{51}$Sb isotopes. When a proton is added to the $Z = 50$ core, the system may favor deformation for a lower total energy. Further, with an unpaired proton, the Hamiltonian of the nucleus is no longer time invariant. The time-odd parts in the mean-field appear. Polarizations of these types are properly taken into account in the blocking calculations [28]. The removal of a level near Fermi surface results in the shrink of pairing gap of the system, which in turn impacts the relative energies among different configurations.

Figure 1 shows Nilsson diagrams with $Z,N \approx 50$ for ^{112}Sn and ^{90}Zr, calculated with UNEDF2 [32] EDF. At each β_2 value, the s.p. levels are obtained by diagonalizing the mean-field Hamiltonian. The orbits at spherical shape are $\pi 1h_{11/2}, \pi 1g_{7/2}$, and $\pi 2d_{5/2}$ above the $Z = 50$ shell gap.

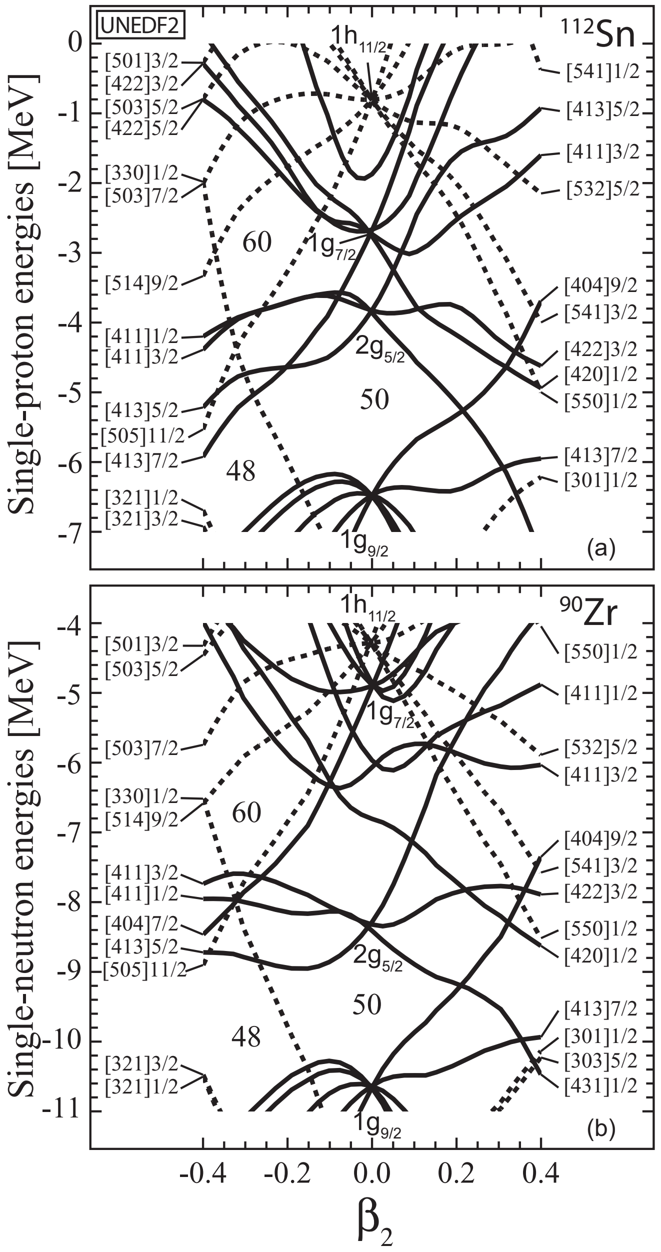

FIG. 1. Mean-field single-proton levels for ^{112}Sn (a) and single-neutron levels for ^{90}Zr (b) as a function of β_2 deformation, calculated with UNEDF2 parametrization. For the definition of β_2, see Ref. [39].

Figure 2(a) displays the energy differences between mean-field orbits $\pi 1h_{11/2}$ and $\pi 1g_{7/2}$ for Sn isotopes. The experimental data are taken from Ref. [5]. Note that the energy differences along the Sb isotopes were obtained by measuring the Triton energies from Sn(α,t)Sb reactions. The respective $\pi 1h_{11/2}$ and $\pi 1g_{7/2}$ origins of the $I^\pi = 11/2^-$ and $7/2^+$ states are determined from the cross sections calculated with distorted-wave Born approximation (DWBA) [5]. The main uncertainty associated with this procedure is the s.p. (quasiparticle) characterizations of $11/2^-$ and $7/2^+$ states, which are concluded from the near-constant (with relative deviation of about 15%) spectroscopic factors from DWBA calculations [5]. From Ref. [22], it is known that these energy differences correspond to the mean-field energy differences only if one assumes that the states are not correlated systems.

It can be seen that, for all the three EDFs, with increasing neutron number the energy differences increase linearly with similar slopes. UNEDF1$^{\text{SO}}$ results give absolute energy differences systematically ≈1.5 MeV lower than those of the original UNEDF1 EDF. This is due to a larger isoscalar SO parameter ($C_0^{\nabla J}$) of UNEDF1$^{\text{SO}}$ [29], which raises $\pi 1g_{7/2}$ and lowers $\pi 1h_{11/2}$, resulting in a much smaller difference between them.

Figure 3(a) shows the differences of the total energies between $\pi 11/2^-[505]$ and $\pi 7/2^+[404]$ states for Sb isotopes.

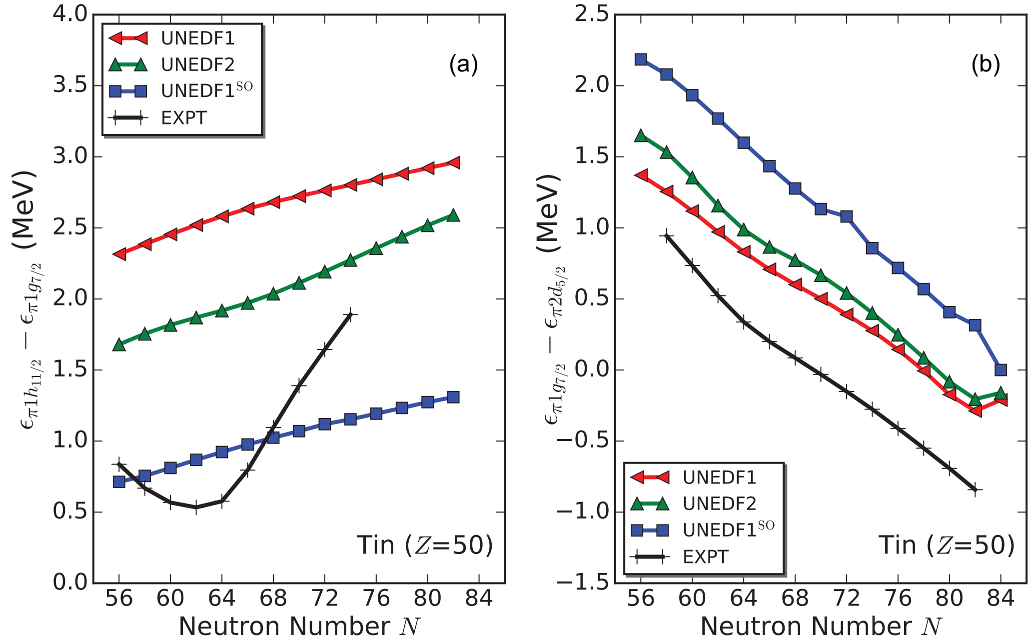

FIG. 2. Energy differences between spherical (a) $\pi 1h_{11/2}$ and $\pi 1g_{9/2}$ shells and between (b) $\pi 1g_{9/2}$ and $\pi 2d_{5/2}$ shells calculated with UNEDF1, UNEDF2, and UNEDF1^{SO} EDFs. Experimental data are taken from Ref. [5].

The total energies for different configurations are obtained by blocking the relevant quasiparticle orbits when solving the HFB equations. It can be seen that the addition of a proton induces sizable oblate deformation ($|\beta_2| \approx 0.1 - 0.2$) for $N = 56$–74. To illustrate the effect of deformation, it is observed that the equilibrium deformations for $11/2^-$ and $7/2^+$ states in ^{117}Sb$_{66}$ is at $\beta_2 \approx -0.17$ [Fig. 3(b)]. From Fig. 1, it can be seen that the energy difference between $\pi 11/2^-$ [505] and $\pi 7/2^+$ [413] is about 1.5 MeV at $\beta_2 \approx -0.17$, which is $\approx$0.5 MeV lower than the gap between $\pi 1h_{11/2}$ and $\pi 1g_{7/2}$ levels at spherical shape. As a result of this polarization effect, in Sn$_{56-74}$ the calculated energy-difference curves in Fig. 3 exhibit dips, which is qualitatively in better agreement with data compared to the mean-field results.

Figure 2(b) shows the energy differences between $\pi 1g_{7/2}$ and $\pi 2d_{5/2}$ for Sn isotopes. The calculations well reproduce the trend and the slope of the experimental data. But the absolute values are overpredicted by 500–600 keV for UNEDF1 and UNEDF2 EDFs. Calculations with UNEDF1^{SO} EDF predict even larger energy differences than the experimental data, due to a higher $\pi 1g_{7/2}$ level resulting from a larger isoscalar SO coupling constant than that of UNEDF1 parametrization.

The total energy differences between $\pi 7/2^+$[404] and $\pi 5/2^+$[402] states with blocked calculations in Sb isotopes are compared with data in Fig. 3(c). For the three EDFs, the energy differences are systematically lower than that of the mean-field values by about 0.5 MeV, bringing UNEDF1 and UNEDF2 values rather close to the data. The effect of deformation is to generate a kink at $N \approx 66$, as shown in Fig. 3(c). It is interesting to note that the experimental data show a change in slope around $N \approx 70$ (see Fig. 1 of Ref. [40]). For heavier isotopes with UNEDF1 and UNEDF1^{SO}, I could not distinguish the two $\pi 5/2^+$ states originating from $\pi 1g_{7/2}$ and $\pi 2d_{5/2}$ orbits from each other. But it can be expected that for those near-spherical systems, the slopes of energy-difference curves should follow those from the mean-field values in Sn isotopes, shown in Fig. 2.

One needs to note that for $_{53}$I and $_{51}$Sb isotopes, excitation energies of $9/2^+$ states were observed to exhibit a parabolic-like dependence on neutron number. This is similar to the case of $11/2^-$ states [41], where the experimental data were well explained in the context of shape coexistence and shape evolution employing a Woods-Saxon mean field with the odd valence proton diabatically blocked when changing the β_2 deformation parameter. In addition, similarities of excitation energy curves between $11/2^-$ states in Sb isotopes and that of 3^- octupole collective states in neighboring Sn isotopes indicate considerable mixing, in Sb isotopes, between quasiparticle $11/2^-$ states and $3^- \otimes 2d_{5/2}$ particle-couple-vibrational states [3].

B. Influence of the tensor part of the Skyrme interaction

In the previous analysis, it is seen that the inclusion of the tensor interaction in the UNEDF2 parametrization does not provide an improved description for the evolution of the s.p. energy difference above the $Z = 50$ shell gap, compared to UNEDF1 and UNEDF1^{SO}, where tensor parts are ignored. In this section, I examine in detail the tensor parameters α_T and β_T (or $C^J_{0,1}$) by varying them around the original UNEDF2 parametrization, with the hope of gaining some insights about how to better constrain the tensor part in future parametrizations.

1. Existing parametrizations in the tensor part

Figure 4 shows a few existing parametrizations in terms of the position of their tensor parameters, C^J_0 and C^J_1.

For parameter labeled with "Skxtb" [8], the parameters of tensor part are obtained by analyzing the energy differences between $\pi 1h_{11/2}$ and $\pi 1g_{9/2}$ spherical shells across the Sn isotopes. For "Colo" [9], the parameters are obtained by

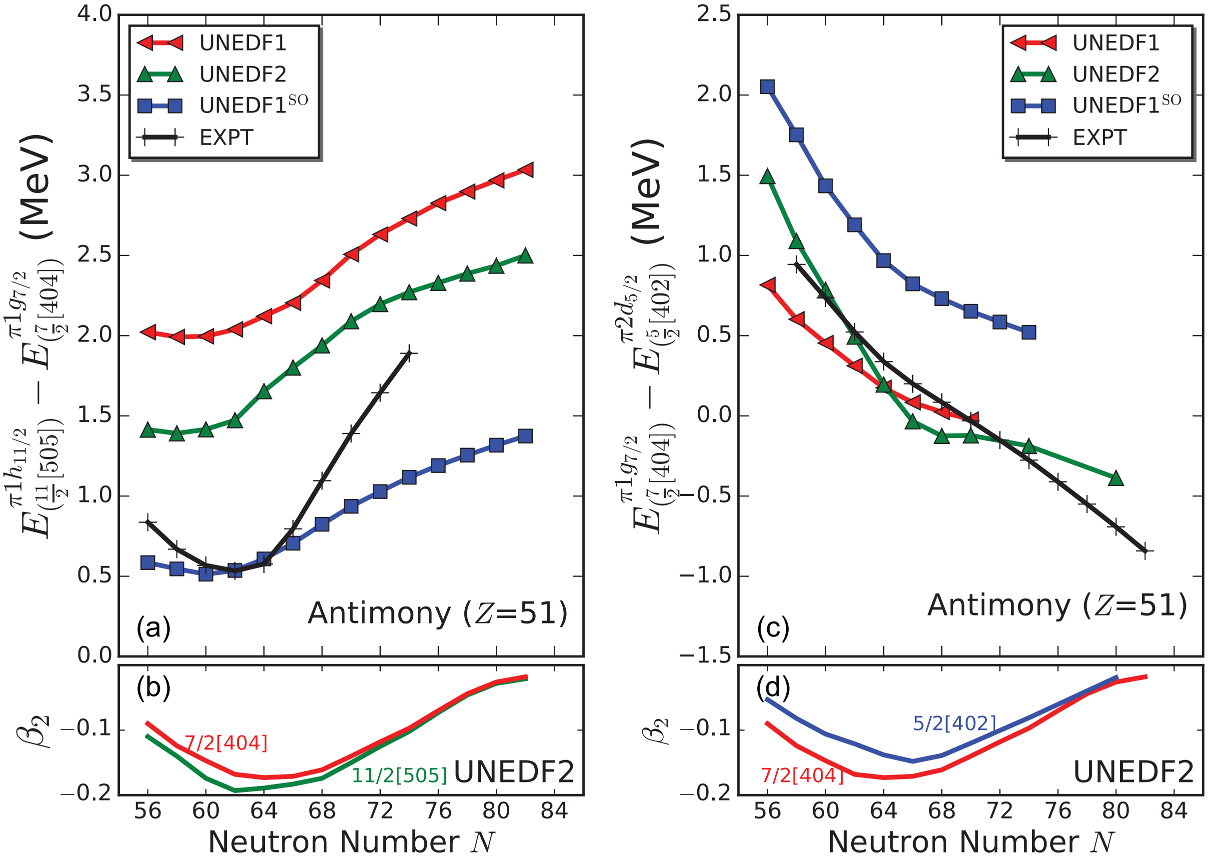

FIG. 3. Total energy differences between (a) $\pi 11/2^-[505]$ and $\pi 7/2^+[404]$ states and between (c) $\pi 7/2^+[404]$ and $\pi 5/2^+[402]$ states for $_{51}$Sb isotopes. Lower panels show (b) β_2 deformations for $\pi 11/2^-[505]$, $\pi 7/2^+[404]$, and (d) $\pi 5/2^+[402]$ states with UNEDF2 for $_{51}$Sb isotopes.

studying the gap between $\pi 1h_{11/2}$ and $\pi 1g_{9/2}$ in Sn isotopes and between $\nu 1i_{13/2}$ and $\nu 1h_{9/2}$ in $N = 82$ isotones. The parameter set labeled with "Brink" [42] is obtained by studying the energy gaps between $\pi 1h_{11/2}$ and $\pi 1g_{9/2}$ in Sn isotopes; the gaps between $\nu 1i_{13/2}$ and $\nu 1h_{9/2}$ in $N = 82$ isotones; and energies of $\pi 2s_{1/2}$ and $\pi 1d_{5/2}$ relative to $\pi 1d_{3/2}$ states in Ca isotopes. Set "T44" [11] is chosen here by noticing its overall better reproduction of the energy differences between $\pi 1h_{11/2}$, and $\pi 1g_{9/2}$ shells in Sn isotopes [11]. It has to be noted that all previous studies are based on spherical mean-field calculations without deformation taken into account. The parameters labeled with "SkO$_T$" [14] are obtained by analyzing the SO splitting data extensively throughout the nuclear chart. The polarization effect is taken into account in this study.

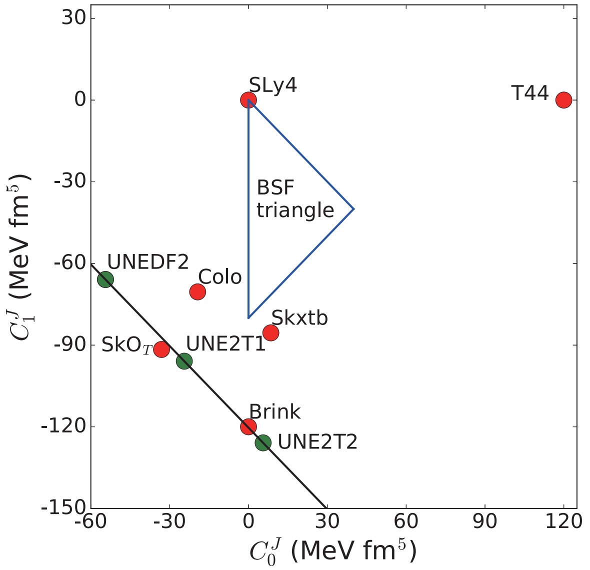

FIG. 4. C_0^J and C_1^J values for selected Skyrme parametrizations [8,9,11,14,42].

2. UNE2T1 and UNE2T2 parametrizations

For UNEDF2, the β_T value ($C_0^J - C_1^J = -11.47$ MeV fm^5) is rather close to zero in the scale of Fig. 4. This explains the similarity in the predictions of the energy difference between UNEDF2 and other EDFs with no tensor interaction included (UNEDF1 and UNEDF1^{SO}) as shown in Figs. 2 and 3.

From Eqs. (11) and (12) I have indicated that, in the tensor sector, β_T parameter governs the strength of the neutron-proton interaction. Indeed, β_T controls how much the SO potential varies for one nucleonic type when the density of the other nucleonic type is changing. In Fig. 4, I show a line with the same α_T value as the original UNEDF2 one, but with different β_T values. Interestingly, one sees that the lower part of the line crosses a region where a few recent new parametrizations

TABLE I. UNE2T1 and UNE2T2 parameters that differ from UNEDF2 parameters.

	UNEDF2	UNE2T1	UNE2T2
C_0^J	−54.433	−24.433	5.567
C_1^J	−65.903	−95.903	−125.903
V_0^n	−208.889	−216.75	−223.50
V_0^p	−230.330	−236.95	−239.20

[8,9,11] proposed that the optimal tensor parameters, α_T and β_T values, should be located.

I use two pairs of parameters that differ from the UNEDF2 in the tensor part by $(\Delta C_0^J, \Delta C_1^J) = (+30, -30)$ MeV fm^5 (denoted with UNE2T1) and $(\Delta C_0^J, \Delta C_1^J) = (+60, -60)$ MeV fm^5 (UNE2T2). The position of these two EDFs is shown in Fig. 4. The current choice of the $C_{0,1}^J$ values is motivated by the following considerations: (1) to minimize the difference from the UNEDF2 parametrization by keeping α_T unchanged and (2) to improve the description of experimental SE in Sn isotopes by varying β_T value toward those existing parameters in the tensor part.

It is known that the size of pairing gaps plays important role in determining the relative excitation energies among configurations near Fermi level. Hence, the pairing strengths of these two parametrizations are readjusted by matching the $(\Delta + \lambda_2)_{n,p}$ values in ^{120}Sn with UNEDF2 parametrization. The resulted parameters that differ from original UNEDF2 EDFs are compared with those of UNEDF2 in Table I. The pairing strengths differ from the respective original values by less than 5%. The difference of excitation energies generated from changed pairing strengths is rather small.

Before presenting the results with UNE2T1 and UNE2T2 EDFs, it is important to examine their predictions for observables such as binding energies, two particle separation energies, and shape-coexistence properties for selected nuclei.

TABLE II. Total energy differences (in MeV) between calculation and experimental data. Calculations are performed with UNEDF2, UNE2T1, and UNE2T2 EDFs for selected nuclei near ^{132}Sn, ^{208}Pb, and ^{254}No. Experimental data are taken from Ref. [43–45].

Nuclei	UNEDF2	UNE2T1	UNE2T2
^{132}Sn	+0.271	−5.001	−9.801
^{130}Sn	+0.611	−3.853	−7.831
^{128}Sn	−0.232	−3.877	−7.040
^{130}Cd	+0.263	−3.922	−7.845
^{128}Cd	−0.052	−3.502	−6.719
^{126}Cd	−1.175	−4.000	−6.536
^{208}Pb	+2.239	−3.578	−8.959
^{206}Pb	+2.305	−3.324	−8.463
^{204}Pb	+1.516	−4.056	−8.955
^{206}Hg	+1.503	−3.894	−8.813
^{204}Hg	+0.693	−4.525	−9.208
^{202}Hg	−0.573	−5.757	−10.248
^{254}No	−1.530	−6.375	−10.290
^{252}No	−0.929	−5.834	−9.690
^{250}No	−0.688	−5.540	−9.257
^{252}Fm	−2.416	−7.222	−10.740
^{250}Fm	−1.661	−6.611	−10.191
^{248}Fm	−1.221	−6.140	−9.734

TABLE III. The differences of two-neutron (ΔS_{2n}) and two-proton (ΔS_{2p}) separation energies (in MeV) between the calculations and experimetal data. Calculations are performed with UNEDF2, UNE2T1, and UNE2T2 EDFs for selected nuclei near ^{132}Sn, ^{208}Pb, and ^{254}No. Experimental data are taken from Refs. [43–45].

Nuclei	ΔS_{2n}			ΔS_{2p}		
	UNEDF2	UNE2T1	UNE2T2	UNEDF2	UNE2T1	UNE2T2
^{132}Sn	−0.341	−1.149	−1.971	+0.004	−1.083	−1.590
^{130}Sn	−0.843	+0.024	−0.791	+0.663	−0.351	−1.112
^{208}Pb	−0.066	−0.257	−0.496	+0.736	+0.316	−0.146
^{206}Pb	+0.789	+0.735	+0.492	+1.612	+1.204	+0.745
^{254}No	−0.604	−0.544	−0.603	+0.884	+0.845	+0.448
^{252}No	−0.269	−0.322	−0.461	+0.732	+0.777	+0.501

Tables II and III list the differences between the calculation and experimental data for the total energies, and the two particle separation energies, respectively, for selected nuclei around ^{132}Sn, ^{208}Pb, and ^{254}No. The differences are obtained with

$$\Delta E_{\text{tot}} = E_{\text{tot}}^{(\text{cal})} - E_{\text{tot}}^{(\text{exp})}, \tag{16}$$

$$\Delta S_{2q} = S_{2q}^{(\text{cal})} - S_{2q}^{(\text{exp})}, \quad q = n, p. \tag{17}$$

The calculated and experimental two particle separation energies are obtained from total energies [45], through

$$S_{2n} = E_{\text{tot}}(Z,N) - E_{\text{tot}}(Z,N-2), \tag{18}$$

$$S_{2p} = E_{\text{tot}}(Z,N) - E_{\text{tot}}(Z-2,N). \tag{19}$$

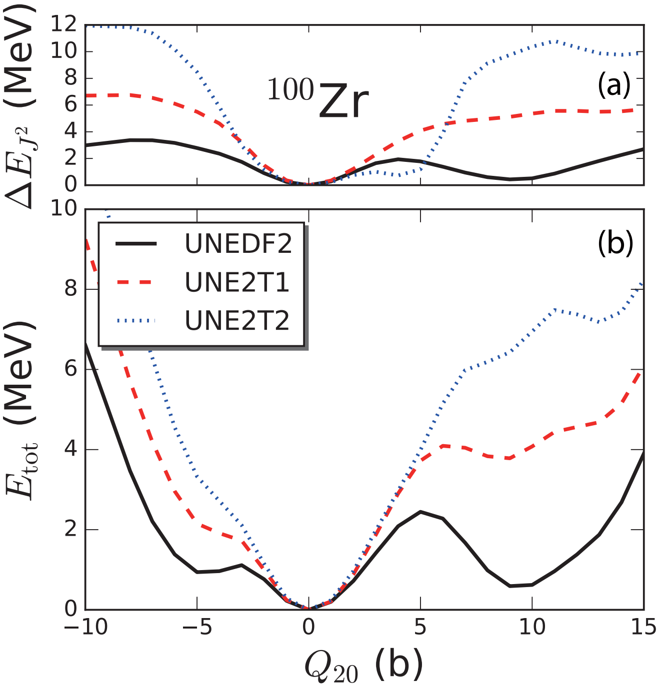

FIG. 5. Energy contribution due to J^2 term (a) and the total energy as a function of Q_{20} for ^{100}Zr calculated with UNEDF2, UNE2T1, and UNE2T2 EDFs.

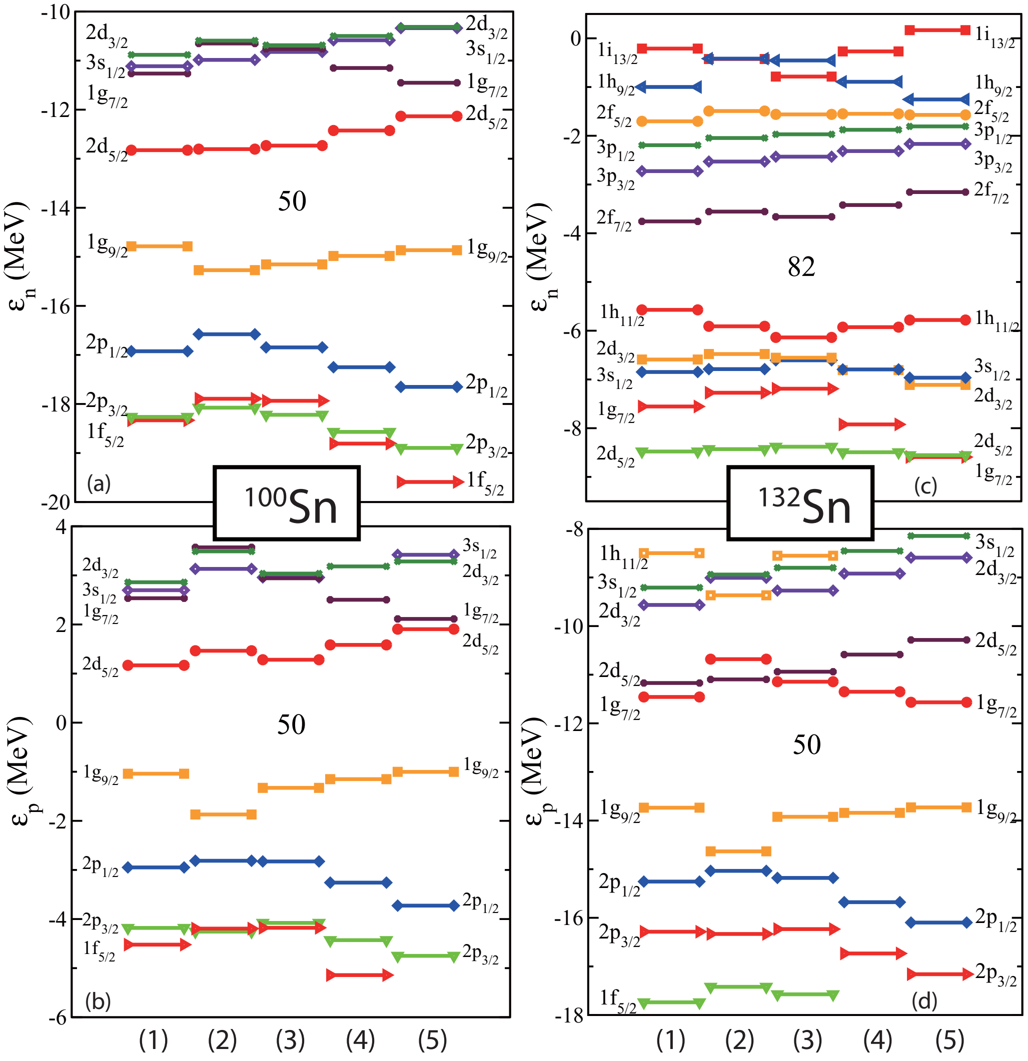

FIG. 6. S.p. spectra for ^{100}Sn and ^{132}Sn, calculated with UNEDF1 (1), UNEDF1$^{\mathrm{SO}}$ (2), UNEDF2 (3), UNE2T1 (4), and UNE2T2 (5) EDFs.

Note that the E_{tot}'s in Eqs. (16) and (18) are absolute and/or positive values.

In Table II, it can be seen that the good agreement between experimental data and calculations with UNEDF2 ($\Delta E_{\mathrm{tot}} \approx 1.5$ MeV) degrades rapidly from UNE2T1 ($\Delta E_{\mathrm{tot}} \approx 6$ MeV), to UNE2T2 ($\Delta E_{\mathrm{tot}} \approx 10$ MeV) EDFs. In Table III, the calculated two-neutron and two-proton separation energies with UNE2T1 and UNE2T2 EDFs differ from the data by $\leqslant 1$ MeV. The deviations is comparable to that of the UNEDF2 parametrizations. For axially deformed No and Fm nuclei near ^{254}No, UNE2T1 and UNE2T2 EDFs predict deformations that are similar to that of UNEDF2 results.

Given the predicted binding energies, UNE2T1 and UNE2T2 EDFs are not suitable for practical predictions. Nevertheless, since the relevant properties of nuclei around double magic nuclei ^{132}Sn and ^{208}Pb were used to determine UNEDF2 parameters [32], ^{132}Sn and ^{208}Pb may be regarded as "anchor" nuclei. The fact that UNE2T1, and UNE2T2 *systematically* underestimate their binding energies with respect to the UNEDF2 results might indicate prospects for general improvements, were the rest of the parameters of UNE2T1 and UNE2T2 readjusted. This is a strategy that has been taken in Ref. [11].

Shape coexistence is another aspect that may be affected by the variation of tensor parameters [12,46,47]. Figure 5 shows the energy curves of ^{100}Zr calculated with UNEDF2, UNE2T1, and UNE2T2. It can be seen that UNEDF2 the parameter predicts two minima at prolate and oblate deformations. The minimum at prolate shape becomes a shoulder for UNE2T1 and disappears for UNE2T2. The oblate minimum of UNEDF2 does not show in UNE2T1 and UNE2T2 results.

Charge radii measurements of Zr isotopes [48] have shown that ^{100}Zr is well deformed in the ground state (g.s.), with $\beta_2 \approx 0.4$. This is rather close to the calculation with UNEDF2 parametrization (in Fig. 5, the prolate minimum at $Q_{20} = 9$ b for UNEDF2 corresponds to $\beta_2 \approx 0.35$), especially after including beyond-mean-field correlations which supposedly favor deformed minimum over the spherical one [49–51].

The energy contribution from the J^2 terms [Eq. (8)] is plotted against Q_{20} in Fig. 5(a). It can be seen that with UNEDF2 the E_{J^2} curve show minima in the spherical and prolate

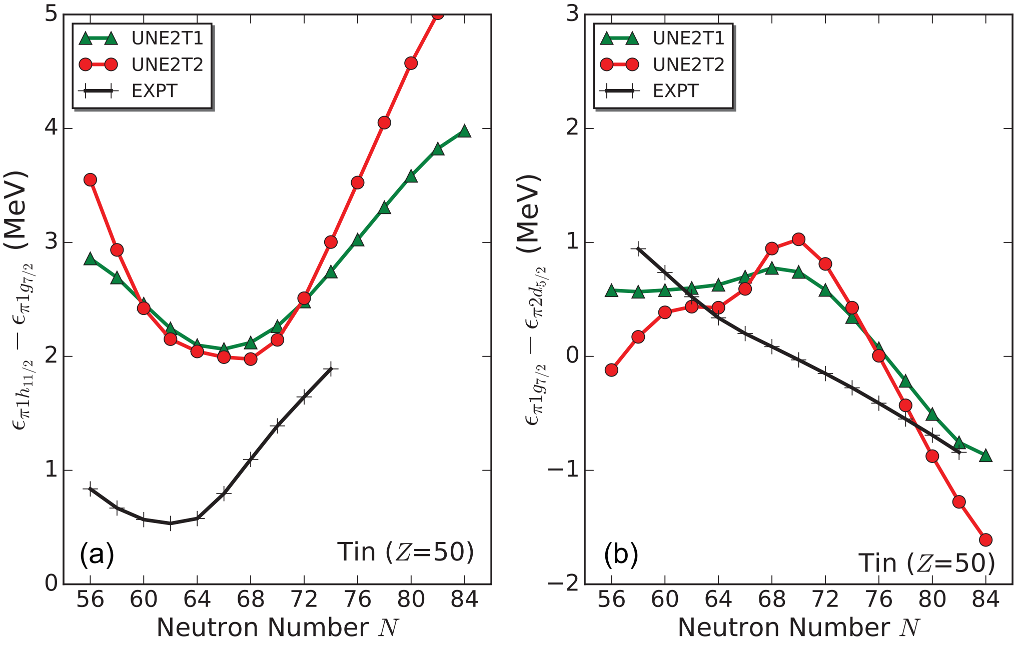

FIG. 7. Same as Fig. 2, except for UNE2T1 and UNE2T2 parameters described in the text.

deformation. Whereas with UNE2T1 and UNE2T2 EDFs, one obtains deeper spherical minima, and the prolate minimum is missing in both parametrizations.

It is useful to compare Fig. 5 with Fig. 27 of Ref. [12], paying attention to the E_{tot} and ΔE_{J^2} curves with parameter pairs: (UNEDF2, UNE2T1), (SLy5, SLy5+T), and (T22/SLy4, T62). These are grouped into pairs since the former parameters in the parentheses are from global fits without paying special attention to tensor parameters, although UNEDF2 and SLy5 contain nonzero tensor terms. The latter parameters are obtained by fixing α_T and β_T values with the remaining parameters readjusted (T62) or unchanged (UNE2T1 and SLy5+T), with respect to the respective former parameters in the parentheses.

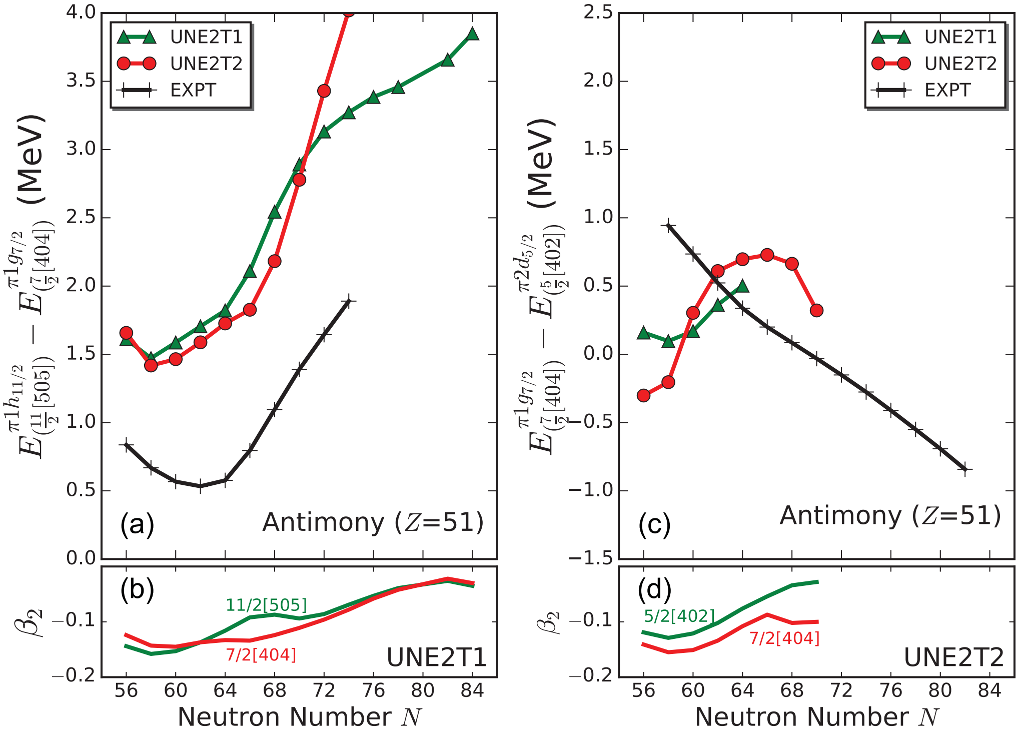

FIG. 8. Same as Fig. 3, except for UNE2T1 and UNE2T2 parameters described in the text.

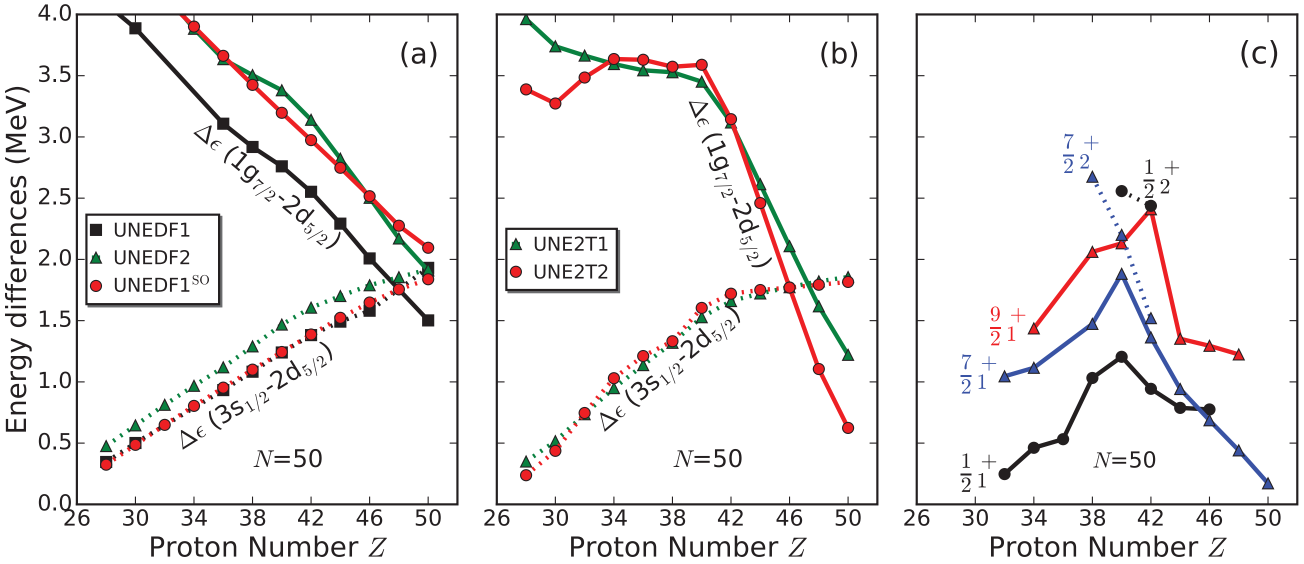

FIG. 9. (a) Mean-field energy differences between $\nu 1g_{7/2}$ and $\nu 2d_{5/2}$ levels and between $\nu 3s_{1/2}$ and $\nu 2d_{5/2}$ levels. (b) Same as in panel (a), but with UNE2T1 and UNE2T2 parametrizations. (c) Experimental data are taken from Ref. [57]. The g.s. are $5/2^+$ states.

The above parameter pairs are giving similar curves in the sense that (1) the former parameter sets in the parentheses predict soft $E_{\rm tot}$ and ΔE_{J^2} curves (for T22/SLy4, ΔE_{J^2} vanishes), whereas the latter parametrizations enhance the spherical one; (2) the latter parameter sets in the parentheses moves tensor parameters (C_0^J, C_1^J) to the "southeast" corner of Fig. 4, with respect to the former parameters in the parentheses (see also Fig. 1 of Ref. [12]). However, T62 differs from UNE2T1 and SLy5+T in that the rest of the parameters except for $C_{0,1}^J$ have been readjusted. This indicates that a readjustment may not be able to result in prolate minimum for UNE2T1 or UNE2T2 either.

The landscape of total nuclear energy versus various deformation parameters is closely related to the underlying s.p. structure. From a perspective of the macroscopic-microscopic methods [2,52], the effect of nonuniformities of s.p. levels can be evaluated by extracting the oscillating part ($E_{\rm osc}$) [2] of the total energy, through a Strutinsky procedure [52–55]. Although in the present calculated spectra (see Fig. 6 in the spherical case), the effect of changing s.p. level densities on

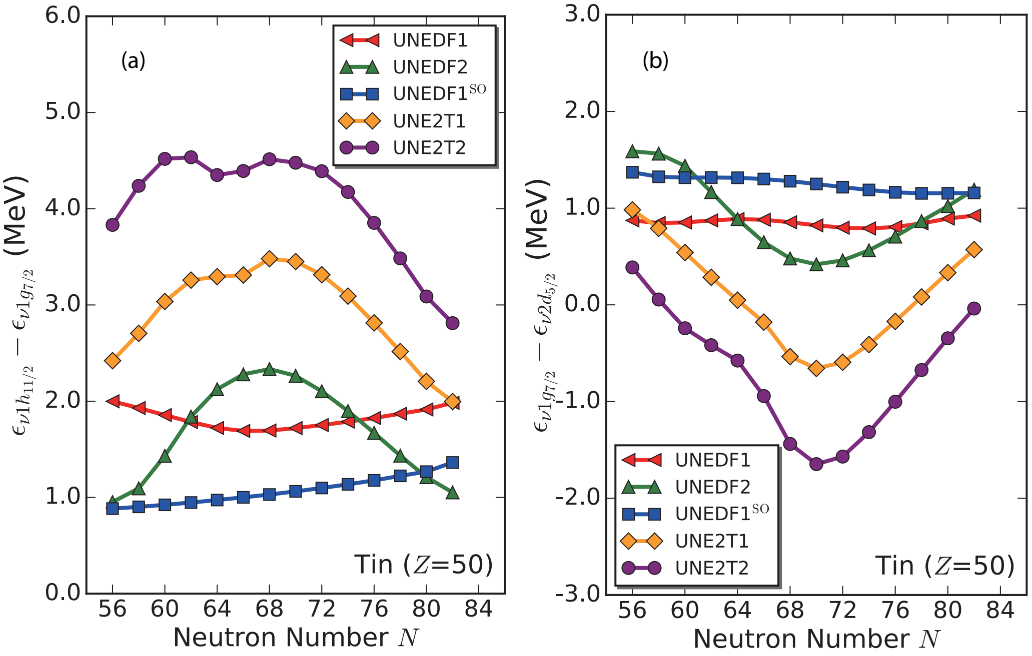

FIG. 10. Mean-field energy differences (a) between $\nu 1h_{11/2}$ and $\nu 1g_{7/2}$ levels and (b) between $\nu 1g_{7/2}$ and $\nu 2d_{5/2}$ levels calculated with various EDFs.

E_{osc} is not obvious, a realistic calculation of E_{osc} as a function of tensor parameters may provide key information about the formation of local minima, and thus about how to further constrain the tensor parameters. These studies are outside the scope of the present work.

3. Results for SE above $Z = 50$ gap

Figure 6 compares the s.p. spectra calculated by UNE2T1 and UNE2T2 with those calculated by UNEDF1, UNEDF1$^{\mathrm{SO}}$, and UNEDF2 for ^{100}Sn and ^{132}Sn. Interestingly, similarities between the spectra with UNEDF2 and UNEDF1$^{\mathrm{SO}}$ can be seen, except for proton levels of ^{132}Sn. By comparing s.p. levels from UNE2T1 and UNE2T2 with those of UNEDF2, smooth variations of levels around $N = 82$ and $Z = 50$ shell gaps can be seen.

It is observed from Fig. 7(a) that the trend of the energy-difference curve is very well reproduced by UNE2T1. Similar results were obtained in Refs. [9,11,56]. However, in Fig. 7(b) one sees that UNE2T1 and UNE2T2 both fail to reproduce the general trend and the slope of the curve of the experimental energy difference between $\pi 1g_{7/2}$ and $\pi 2d_{5/2}$. Taking into account deformation, in Fig. 8, it is shown that the $\pi 1h_{11/2}$ and $\pi 1g_{9/2}$ are better reproduced, but the energy-difference curve between $\pi 1g_{7/2}$ and $\pi 2d_{5/2}$ is qualitatively at variance with experimental data.

4. Results for SE above $N = 50$ gap

To see the performance of the new tensor parameters, Fig. 9 shows the energy differences between $\nu 1g_{7/2}$ and $\nu 2d_{5/2}$ states, and between $\nu 3s_{1/2}$ and $\nu 2d_{5/2}$ states for $N = 50$ isotones, calculated with UNEDF1, UNEDF2, UNEDF1$^{\mathrm{SO}}$, UNE2T1, and UNE2T2 EDFs. The blocking calculations predict near-spherical shape for $1/2^+$ and $5/2^+$ states. This makes it rather difficult to distinguish $1/2^+$ and $5/2^+$ states from other states with the same Ω values. Hence, in the present calculation, only mean-field results are shown. It should be noted that $\nu 7/2[404]$ and $\nu 11/2[505]$ states are calculated to be well deformed ($\beta_2 \approx -0.2$).

Available experimental data are displayed in Fig. 9(c). Experimentally, the determination of s.p. character for each state is by no means trivial. Here I adopt the assignment of Ref. [3] (see discussions of Fig. 30 in Ref. [3]). Specifically, the $7/2_1^+$ states for heavier isotones ($Z > 44$) and $1/2_1^+$ states for lighter isotones ($Z < 38$) are considered to be mostly of s.p. character. It is seen in Fig. 9(c) that the $1/2_1^+$ states (for $Z < 38$) increase and the $7/2_1^+$ states (for $Z > 44$) decrease in energy with proton number. This is qualitatively in agreement with the calculations [see Figs. 9(a) and 9(b)], which overestimates the proton number where the $1/2^+$ and $7/2^+$ states cross each other. It has to be noted that, after incorporating pairing correlation, the excitation of both states will decrease, as shown in Figs. 2 and 3.

In Fig. 9(b), with UNE2T1 and UNE2T2, the energy differences between $\nu 3s_{1/2}$ and $\nu 2d_{5/2}$ states increase with proton number and saturate at $Z = 42$. The energies of $\nu 1g_{7/2}$ states increase with decreasing proton number and saturate at $Z = 40$. These plateaus are absent using EDFs without tensor terms, as shown in Fig. 9(a). Interestingly, the experimental excitation energies of $1/2_1^+$ states for $Z > 44$ seem to show a plateau [see Fig. 9(c)]. The situation of $7/2_1^+$ states in lighter $N = 50$ isotones ($Z < 38$) is difficult to summarize as they are possibly mixed with $7/2_2^+$ states. Future experimental findings about the excitation energies of the $1/2^+$ and $7/2^+$ states in these $N = 50$ isotones may reveal more details about the tensor interactions.

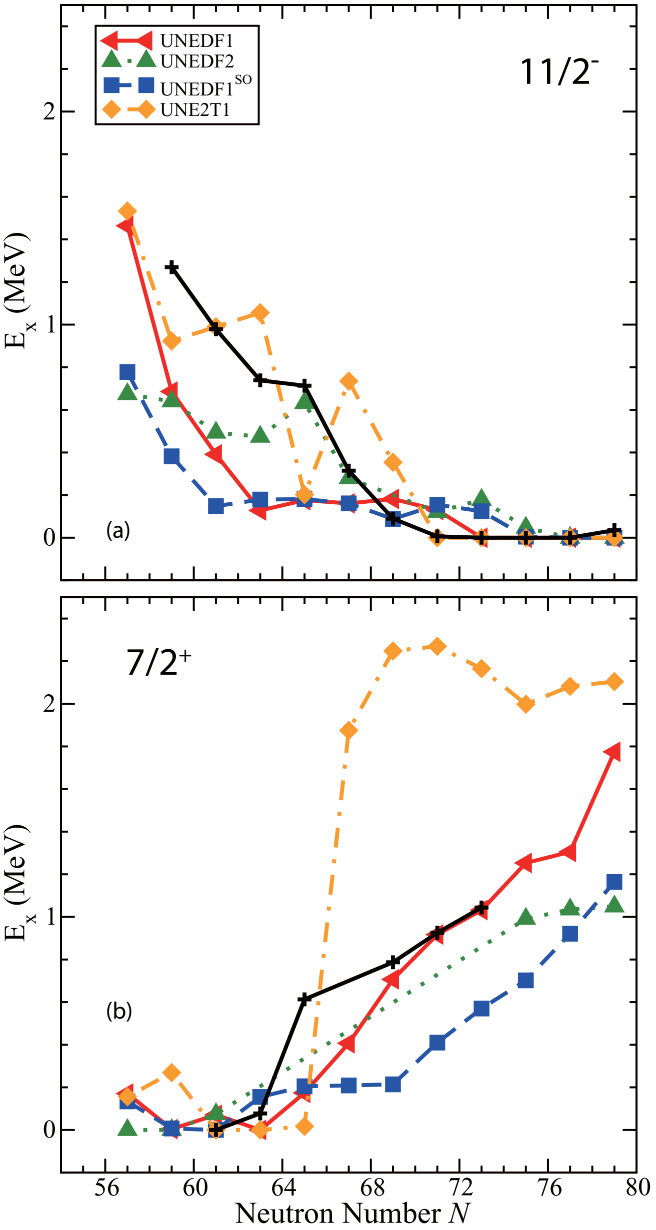

FIG. 11. Excitation energies of neutron $\frac{11}{2}^-$ (a) and $\frac{7}{2}^+$ (b) states in Sn isotopes, calculated with various EDFs. The experimental data (crosses) are taken from Ref. [57]. See text for details about configuration assignments.

5. Results for neutron SE as a function of neutron number in Sn isotopes

To my knowledge, the existing studies focus on the SE above certain shell gap of given nucleonic type, as varying

TABLE IV. Calculated excitation energies (in MeV) of $11/2^-$ and $7/2^+$ in $^{107-129}$Sn with UNEDF1, UNEDF2, UNEDF1$^{\mathrm{SO}}$, UNE2T1, and UNE2T2. The experimental values are taken from Ref. [57].

Nucleus	Config.	UNEDF1		UNEDF1$^{\mathrm{SO}}$		UNEDF2		UNE2T1		UNE2T2		Expt.
		E_x	β_2	E_x	β_2	E_x	β_2	E_x	β_2	E_x	β_2	(MeV)
^{107}Sn	$\nu\frac{11}{2}^-[505]$	1.464	−0.125	0.778	−0.084	0.674	−0.058	1.533	−0.146	1.982	−0.172	
	$\nu\frac{7}{2}^+[404]$	0.171	−0.058	0.134	−0.054	0.0	−0.046	0.156	−0.053	1.067	−0.091	
^{109}Sn	$\nu\frac{11}{2}^-[505]$	0.686	−0.141	0.382	−0.102	0.640	−0.086	0.923	−0.173	1.279	−0.189	1.2698
	$\nu\frac{7}{2}^+[404]$	0.004	−0.042	0.007	−0.052	0.0	−0.034	0.269	−0.021	1.803	−0.031	
^{111}Sn	$\nu\frac{11}{2}^-[505]$	0.391	−0.141	0.148	−0.113	0.493	−0.122	0.990	−0.163	1.308	−0.174	0.9786
	$\nu\frac{7}{2}^+[404]$	0.071	+0.025	0.0	−0.042	0.074	+0.005	0.0	+0.077	0.371	+0.091	0.0
^{113}Sn	$\nu\frac{11}{2}^-[505]$	0.128	−0.134	0.179	−0.114	0.474	−0.127	1.056	−0.143	1.417	−0.151	0.7384
	$\nu\frac{7}{2}^+[404]$	0.0	+0.056	0.155	−0.002			0.0	+0.058	0.278	+0.060	0.0774
^{115}Sn	$\nu\frac{11}{2}^-[505]$	0.176	−0.118	0.181	−0.105	0.633	−0.112	0.202	−0.114	1.304	−0.116	0.7136
	$\nu\frac{7}{2}^+[404]$	0.174	+0.063	0.205	+0.052			0.017	+0.054	1.127	+0.054	0.6128
^{117}Sn	$\nu\frac{11}{2}^-[505]$	0.161	−0.093	0.161	−0.086	0.279	−0.085	0.735	−0.076	1.093	−0.075	0.03146
	$\nu\frac{7}{2}^+[404]$	0.407	+0.070	0.209	+0.070			1.875	+0.054	2.616	+0.046	
^{119}Sn	$\nu\frac{11}{2}^-[505]$	0.182	−0.065	0.088	−0.059			0.354	−0.050	0.625	−0.048	0.0895
	$\nu\frac{7}{2}^+[404]$	0.707	+0.074	0.214	+0.076			2.248	+0.056	3.145	+0.035	0.787
^{121}Sn	$\nu\frac{11}{2}^-[505]$	0.130	−0.036	0.155	−0.027	0.121	−0.039	0.0	−0.031	0.0	−0.029	0.0063
	$\nu\frac{7}{2}^+[404]$	0.917	+0.074	0.410	+0.071			2.270	+0.087	3.273	+0.034	0.9256
^{123}Sn	$\nu\frac{11}{2}^-[505]$	0.0	−0.016	0.124	−0.006	0.178	−0.017	0.0	−0.018	0.0	−0.018	0.0
	$\nu\frac{7}{2}^+[404]$	1.032	+0.068	0.570	+0.060			2.165	+0.099	3.044	−0.026	1.044
^{125}Sn	$\nu\frac{11}{2}^-[505]$	0.0	−0.002	0.005	+0.005	0.049	0.0	0.0	−0.004	0.0	−0.007	0.0
	$\nu\frac{7}{2}^+[404]$	1.253	+0.058	0.702	+0.047	0.991	+0.080	1.998	+0.083	2.775	−0.024	
^{127}Sn	$\nu\frac{11}{2}^-[505]$	0.0	+0.013	0.0	+0.013	0.0	+0.013	0.0	+0.010	0.0	+0.012	0.0
	$\nu\frac{7}{2}^+[404]$	1.305	+0.038	0.921	+0.037	1.035	+0.038	2.082	+0.051	2.900	−0.011	
^{129}Sn	$\nu\frac{11}{2}^-[505]$	0.0	+0.018	0.0	+0.018	0.0	+0.019	0.0	+0.020	0.0	+0.024	0.0352
	$\nu\frac{7}{2}^+[404]$	1.775	+0.035	1.164	+0.029	1.049	+0.026	2.104	+0.028	3.174	+0.014	

the other nucleonic type. This is probably due to (1) the difficulties of systematic experimental characterization of s.p. (quasiparticle) states and (2) the difficulties in singling out tensor contribution theoretically. However, this results in the α_T tensor parameter underdetermined [21]. To learn more about α_T, I study the neutron SE as a function of neutron number in Sn isotopes.

Figure 10 shows the s.p. energy differences for Sn isotopes between $\nu 1h_{11/2}$ and $\nu 1g_{7/2}$ and between $\nu 1g_{7/2}$ and $\nu 2d_{5/2}$ calculated with various EDFs. Compared to Fig. 2, where curves with UNEDF2 show monotonic behavior which is similar to those curves calculated with EDFs with no tensor parts, it can be seen that energy difference curves with UNEDF2 now exhibit bumps and dips around $N = 68$. This is due to the nonzero α_T of UNEDF2, although its β_T is close to zero.

Experimentally, low-energy spectra of odd-A Sn nuclei are known to be complicated, where configuration assignments of bandheads are exceptionally difficult. Fortunately, from Ref. [57], isomeric states with finite half-lives ($\geqslant$1 ns) are systematically observed. For instance, $I^\pi = 11/2^-$ and $7/2^+$ states are yrast, and hence are less mixed with other low-spin states. Consequently, in the present blocking calculations, they correspond to states with $\nu 11/2^-[505]$ and $\nu 7/2^+[404]$ originating from $\nu 1h_{11/2}$ and $\nu 1g_{9/2}$ spherical states, respectively.

Figure 11 compares the experimental data with the blocked calculations with various EDFs. Table IV lists the energies plotted in Fig. 11. The missing results in ^{131,133}Sn which are not shown in the table and figure are due to the difficulties of obtaining convergent solutions. However, it can be seen that ^{127,129}Sn are close to spherical shape. Special attention should be paid to the deformation of $11/2^-$ ($\sim$−0.15) states for lighter isotopes. For $7/2^+$ states, the weak deformation varies from a negative value to a positive one, as the character of s.p. level $7/2^+[404]$ changes from particle to hole state with increasing neutron number.

Experimentally, the energies of $11/2^-$ states decrease with neutron number and become g.s. in ^{121}Sn; the energies of $7/2^+$ increase from close to g.s. to about 1 MeV at $N \approx 75$. These two curves cross each other at $N \approx 65$. The calculations with UNEDF1, UNEDF1$^{\mathrm{SO}}$, and UNEDF2 well reproduce the data. Results of UNE2T1 and UNE2T2 overpredict the energies of $11/2^-$ for $N \geqslant 70$. This is due to the overall larger value of $\Delta e(\nu 1h_{11/2} - \nu 1g_{7/2})$ UNE2T1 and UNE2T2 give, which is shown in Fig. 10(a). It can be expected that a readjustment of the rest of the parameter, especially the SO terms, would bring the curves of UNE2T1 and UNE2T2 close to that of UNEDF2.

It is interesting to compare the results of UNEDF2 and UNE2T1 with those without tensor terms, namely, UNEDF1 and UNEDF1$^{\mathrm{SO}}$. For EDFs without tensor terms, the energies of $7/2^+$ increase monotonically with neutron number for

$N \geqslant 69$, while UNEDF2 and UNE2T1 predict sudden rise of $7/2^+$ energies around $N = 65$ and then the energies saturate as approaching $N = 82$. The data seem to flatten at higher neutron numbers. Experimental excitation energies of $11/2^-$ and $7/2^+$ states close to $N = 82$ are highly desired to determine α_T tensor parameter.

IV. CONCLUSIONS

In summary, I applied Skyrme density-functional theory to the description of shell evolution above the $Z,N = 50$ magic numbers along isotopic and isotonic chains, using UNEDF1, UNEDF2, and UNEDF1$^{\text{SO}}$ EDFs.

For Sn isotopes, the predicted energy differences between $\pi 1h_{11/2}$ and $\pi 1g_{7/2}$ orbits and between $\pi 1g_{7/2}$ and $\pi 2d_{5/2}$ orbits show general qualitative agreement with experimental data.

For $Z = 51$ isotopes, I performed detailed blocked calculations. Comparing the blocked results with the simple mean-field estimates, it was found that blocking those high-Ω oblate-deformation-driving orbits resulted in finite oblate deformation for midshell nuclei. This gave improved agreement with data both qualitatively and quantitatively.

I examined the tensor part of UNEDF2 parametrization. By keeping α_T constant and increasing tensor parameter, β_T, by 60 MeV fm^5 (UNE2T1), both mean-field and blocked results reproduced well the observed trend of energy differences between $\pi 1h_{11/2}$ and $\pi 1g_{7/2}$ orbits in Sb isotopes. However, with UNE2T1, the predicted SE between $\pi 1g_{7/2}$ and $\pi 2d_{5/2}$ states was qualitatively at variance with experimental data.

For $N = 50$ isotones, the variation of experimental excitation energies between $\nu 3s_{1/2}$ and $\nu 1g_{7/2}$ was consistent with the mean-field energy differences calculated with UNE2T1 EDF. The SE in $N = 50$ isotones may represent another interesting testing ground for the study of tensor interaction.

To study the influence of α_T parameter, I calculated the neutron s.p. SE along odd-A Sn isotopes. Due to nonzero α_T, SE with UNEDF2 show behavior that was different from those using EDFs without tensor terms.

I compared the calculated excitation energies of $11/2^-$ and $7/2^+$ states with experimental data. Close to the heaviest isotopes, UNEDF2, and UNE2T1 EDFs predicted energy curves of $7/2^+$ states that were flattened as a function of neutron number, whereas those energy curves resulted from EDFs without tensor terms showed monotonic increase with neutron number. Experimental energies of $7/2^+$ close to ^{132}Sn would reveal detailed information of α_T parameter.

ACKNOWLEDGMENTS

I thank W. Nazarewicz for useful comments and discussions. This work was supported by the US Department of Energy, Office of Science, Office of Nuclear Physics under Award No. DE-SC0008511 (NUCLEI SciDAC Collaboration), Academy of Finland and University of Jyväskylä within the FIDIPRO programme, and Centre of Excellence Programme 2012–2017 (Nuclear and Accelerator Based Physics Programme at JYFL). The CSC-IT Center for Science Ltd., Finland, is acknowledged for the allocation of computational resources.

---

[1] M. Göppert-Mayer, Phys. Rev. **75**, 1969 (1949); **78**, 16 (1950).
[2] P. Ring and P. Schuck, *The Nuclear Many-Body Problem* (Springer-Verlag, Berlin, 1980).
[3] O. Sorlin and M.-G. Porquet, Prog. Part. Nucl. Phys. **61**, 602 (2008).
[4] A. Gade and T. Glasmacher, Prog. Part. Nucl. Phys. **60**, 161 (2008).
[5] J. P. Schiffer, S. J. Freeman, J. A. Caggiano, C. Deibel, A. Heinz, C.-L. Jiang, R. Lewis, A. Parikh, P. D. Parker, K. E. Rehm, S. Sinha, and J. S. Thomas, Phys. Rev. Lett. **92**, 162501 (2004).
[6] T. Otsuka, T. Suzuki, R. Fujimoto, H. Grawe, and Y. Akaish, Phys. Rev. Lett. **95**, 232502 (2005).
[7] T. Otsuka, T. Matsuo, and D. Abe, Phys. Rev. Lett. **97**, 162501 (2006).
[8] B.A. Brown, T. Duguet, T. Otsuka, D. Abe, and T. Suzuki, Phys. Rev. C **74**, 061303(R) (2006).
[9] G. Colò, H. Sagawa, S. Fracasso, and P. F. Bortignon, Phys. Lett. B **646**, 227 (2007).
[10] W. Zou, G. Colò, Z. Ma, H. Sagawa, and P. F. Bortignon, Phys. Rev. C **77**, 014314 (2008).
[11] T. Lesinski, M. Bender, K. Bennaceur, T. Duguet, and J. Meyer, Phys. Rev. C **76**, 014312 (2007).
[12] M. Bender, K. Bennaceur, T. Duguet, P. H. Heenen, T. Lesinski, and J. Meyer, Phys. Rev. C **80**, 064302 (2009).
[13] V. Hellemans, P.-H. Heenen, and M. Bender, Phys. Rev. C **85**, 014326 (2012).
[14] M. Zalewski, J. Dobaczewski, W. Satuła, and T. R. Werner, Phys. Rev. C **77**, 024316 (2008).
[15] M. Zalewski, P. Olbratowski, M. Rafalski, W. Satuła, T. R. Werner, and R. A. Wyss, Phys. Rev. C **80**, 064307 (2009).
[16] J. Dobaczewski, N. Michel, W. Nazarewicz, M. Płoszajczak, and J. Rotureau, Prog. Part. Nucl. Phys. **59**, 432 (2007).
[17] C. Bai, H. Sagawa, H. Zhang, X. Zhang, G. Coló, and F. Xu, Phys. Lett. B **675**, 28 (2009).
[18] C. L. Bai, H. Q. Zhang, H. Sagawa, X. Z. Zhang, G. Colò, and F. R. Xu, Phys. Rev. Lett. **105**, 072501 (2010).
[19] C. L. Bai, H. Q. Zhang, H. Sagawa, X. Z. Zhang, G. Colò, and F. R. Xu, Phys. Rev. C **83**, 054316 (2011).
[20] C. L. Bai, H. Sagawa, G. Colò, H. Q. Zhang, and X. Z. Zhang, Phys. Rev. C **84**, 044329 (2011).
[21] H. Sagawa and G. Colò, Prog. Part. Nucl. Phys. **76**, 76 (2014).
[22] T. Duguet and G. Hagen, Phys. Rev. C **85**, 034330 (2012).
[23] W. Nazarewicz, M.A. Riley, and J. D. Garrett, Nucl. Phys. **A512**, 61 (1990).
[24] W. Nazarewicz, Nucl. Phys. **A574**, 27c (1994).
[25] W. Satuła, J. Dobaczewski, J. Dudek, and W. Nazarewicz, Phys. Rev. Lett. **77**, 5182 (1996).
[26] M. V. Stoitsov, N. Schunck, M. Kortelainen, N. Michel, H. Namb, E. Olsen, J. Sarich, and S. Wild, Comput. Phys. Commun. **184**, 1592 (2013).
[27] J. Dobaczewski and J. Dudek, Phys. Rev. C **52**, 1827 (1995).

[28] N. Schunck, J. Dobaczewski, J. McDonnell, J. Moré, W. Nazarewicz, J. Sarich, and M. V. Stoitsov, Phys. Rev. C **81**, 024316 (2010).

[29] Y. Shi, J. Dobaczewski, and P. T. Greenlees, Phys. Rev. C **89**, 034309 (2014).

[30] M. Bender, J. Dobaczewski, J. Engel, and W. Nazarewicz, Phys. Rev. C **65**, 054322 (2002).

[31] M. Kortelainen, J. McDonnell, W. Nazarewicz, P.-G. Reinhard, J. Sarich, N. Schunck, M. V. Stoitsov, and S. M. Wild, Phys. Rev. C **85**, 024304 (2012).

[32] M. Kortelainen, J. McDonnell, W. Nazarewicz, E. Olsen, P.-G. Reinhard, J. Sarich, N. Schunck, S. M. Wild, D. Davesne, J. Erler, and A. Pastore, Phys. Rev. C **89**, 054314 (2014).

[33] E. Perlińska, S. G. Rohoziński, J. Dobaczewski, and W. Nazarewicz, Phys. Rev. C **69**, 014316 (2004).

[34] Y. M. Engel, D. M. Brink, K. Goeke, S. J. Krieger, and D. Vautherin, Nucl. Phys. A **249**, 215 (1975).

[35] T. Skyrme, Phil. Mag. **1**, 1043 (1956).

[36] T. Skyrme, Nucl. Phys. **9**, 615 (1959).

[37] J. Dobaczewski, I. Hamamoto, W. Nazarewicz, and J. A. Sheikh, Phys. Rev. Lett. **72**, 981 (1994).

[38] J. Meng and I. Tanihata, Nucl. Phys. **650**, 176 (1999).

[39] W. Ryssens, V. Hellemans, M. Bender, and P.-H. Heenen, Comput. Phys. Commun. **187**, 175 (2015).

[40] M.-G. Porquet, S. Péru, and M. Girod, Eur. Phys. J. A **25**, 319 (2005).

[41] K. Heyde, P. V. Isacker, M. Waroquier, J. Wood, and R. Meyer, Phys. Rep. **102**, 291 (1983).

[42] D. M. Brink and F. Stancu, Phys. Rev. C **75**, 064311 (2007).

[43] G. Audi, F. Kondev, M. Wang, B. Pfeiffer, X. Sun, J. Blachot, and M.MacCormick, Chin. Phys. C **36**, 1157 (2012).

[44] G. Audi, M. Wang, A. Wapstra, F. Kondev, M. MacCormick, X. Xu, and B. Pfeiffer, Chin. Phys. C **36**, 1287 (2012).

[45] M. Wang, G. Audi, A. Wapstra, F. Kondev, M. MacCormick, X. Xu, and B. Pfeiffer, Chin. Phys. C **36**, 1603 (2012).

[46] A. Li, E. Hiyama, X.-R. Zhou, and H. Sagawa, Phys. Rev. C **87**, 014333 (2013).

[47] A. Li, X. R. Zhou, and H. Sagawa, Prog. Theor. Exp. Phys. **2013**, 063D03 (2013).

[48] P. Campbell, H. L. Thayer, J. Billowes, P. Dendooven, K. T. Flanagan, D. H. Forest, J. A. R. Griffith, J. Huikari, A. Jokinen, R. Moore, A. Nieminen, G. Tungate, S. Zemlyanoi, and J. Äystö, Phys. Rev. Lett. **89**, 082501 (2002).

[49] T. Duguet, M. Bender, P. Bonche, and P.-H. Heenen, Phys. Lett. B **559**, 201 (2003).

[50] M. Bender, P. Bonche, T. Duguet, and P.-H. Heenen, Phys. Rev. C **69**, 064303 (2004).

[51] J. M. Yao, M. Bender, and P.-H. Heenen, Phys. Rev. C **87**, 034322 (2013).

[52] S. G. Nilsson and I. Ragnarsson, *Shapes and Shells in Nuclear Structure* (Cambridge University Press, Cambridge, UK, 1995).

[53] M. Brack, J. Damgaard, A. S. Jensen, H. C. Pauli, V. M. Strutinsky, and C. Y. Wong, Rev. Mod. Phys. **44**, 320 (1972).

[54] P.-G. Reinhard, M. Bender, W. Nazarewicz, and T. Vertse, Phys. Rev. C **73**, 014309 (2006).

[55] N. Nikolov, N. Schunck, W. Nazarewicz, M. Bender, and J. Pei, Phys. Rev. C **83**, 034305 (2011).

[56] Y. Z. Wang, J. Z. Gu, J. M. Dong, and X. Z. Zhang, Phys. Rev. C **83**, 054305 (2011).

[57] Evaluated Nuclear Structure Data File (ENSDF), Brookhaven National Laboratory, http://www.nndc.bnl.gov/ensdf/.